

# Influence of the core hole on $K\beta$ emission following photoionization or orbital electron capture: A comparison using MnO and $^{55}\text{Fe}_2\text{O}_3$

P. Glatzel

*Department of Applied Science, University of California at Davis, Davis, California 95616*

U. Bergmann

*Physical Biosciences Division, Lawrence Berkeley National Laboratory, Berkeley, California 94720*

F. M. F. de Groot

*Department of Inorganic Chemistry and Catalysis, Utrecht University, Sorbonnelaan 16, 3584 CA Utrecht, The Netherlands*

S. P. Cramer

*Physical Biosciences Division, Lawrence Berkeley National Laboratory, Berkeley, California 94720 and Department of Applied Science, University of California at Davis, Davis, California 95616*

(Received 11 December 2000; published 2 July 2001)

The Mn  $K\beta$  fluorescence emission in MnO after photoionization and in  $^{55}\text{Fe}_2\text{O}_3$  after radioactive electron capture decay from the  $K$  shell have been measured using a crystal array spectrometer with an instrumental energy bandwidth of 0.7 eV (full width at half maximum). Both compounds have a  $3d^5$  valence electron configuration in the ionic approximation. It is found that the spectral features after  $K$  capture in  $^{55}\text{Fe}_2\text{O}_3$  are shifted in emission energy and are sharper, compared to the spectra following photoionization in MnO, i.e., the spectra exhibit a dependence on the mode of excitation. Crystal-field multiplet calculations including ligand-to-metal charge transfer have been carried out for the  $1s$  intermediate states as well as for the  $3p$  to  $1s$  ( $K\beta$ ) radiative transition. The populated  $1s$  intermediate states after photoionization are found to be spread over several eV. In comparison, only the lowest-lying  $1s$  intermediate states split by the weak ( $1s,3d$ ) exchange interaction are populated after  $K$  capture. It is proposed that the differences in population of the  $1s$  intermediate states together with a term-dependent final-state lifetime broadening can account for the changes in the spectral shapes due to the different modes of excitation.

DOI: 10.1103/PhysRevB.64.045109

PACS number(s): 71.15.-m

## I. INTRODUCTION

X-ray spectroscopy is an established tool for probing the electronic structure of  $3d$  transition-metal compounds.<sup>1</sup> A number of techniques, such as photoemission spectroscopy, x-ray absorption, and x-ray emission spectroscopy create a hole in an inner shell in order to investigate the valence electron configuration. With a deeper theoretical understanding of the underlying processes, and further improving x-ray sources, sophisticated experiments have been developed (e.g., resonant inelastic scattering, magnetic dichroism<sup>2,3</sup>) that give detailed information on the valence electron configuration. Core-hole x-ray spectroscopy is applied in various fields ranging from materials sciences to biochemistry. Examples are studies on Mn-oxide compounds with perovskite structure that exhibit colossal magnetoresistance (CMR),<sup>4</sup> high- $T_c$  superconductors such as  $\text{YBa}_2\text{Cu}_3\text{O}_7$  (Ref. 5), and metalloproteins like the 4-Mn cluster in the oxygen evolving complex of the transmembrane protein complex *PSII*.<sup>6</sup>

In core-hole spectroscopy, the creation of a vacancy in an inner shell causes a considerable readjustment of the electrons. The ground-state Hamiltonian relaxes into the new Hamiltonian that includes the core hole. The relaxation can occur nonadiabatically yielding a valence electron configuration of the excited state that differs from the valence electron configuration of the ground state. This imposes some difficulties for the interpretation of the spectra if the goal of

the spectroscopy is to gain knowledge on the electronic ground state configuration. In calculations, one has to extend the one-electron picture and include electron correlation. This can be done by considering more than one electron configuration and assuming interaction between the different configurations (CI).<sup>7</sup> The effects of electron correlation in x-ray spectroscopy of  $3d$  transition metals have been studied by several authors and only a few examples are mentioned in the following.

The satellite structure in  $2p$  absorption spectra could successfully be explained within a ligand-to-metal charge-transfer model.<sup>8-11</sup> Taguchi *et al.* calculated the  $3p$  photoemission spectra (XPS), the  $K\beta$  fluorescence emission (XES), and the spin-dependent  $1s$  absorption spectra of different Mn compounds by means of an  $\text{MX}_6$  cluster model including three configurations.<sup>12,13</sup> They treated the  $K\beta$  emission as a coherent second-order optical process and emphasized the influence of the core-hole potential on the  $1s$  excitation spectra. Kawai *et al.* analyzed the charge-transfer effect on the linewidth of Fe  $K\alpha$  lines using a spin-unrestricted DV- $X\alpha$  molecular-orbital calculation.<sup>14</sup> They calculated the effective number of unpaired electrons in the ground state and in the presence of a  $1s$  hole and obtained similar numbers for the excited states of FeO and  $\text{Fe}_2\text{O}_3$  giving rise to almost identical  $K\alpha$  fluorescence emission. Von dem Borne and collaborators performed  $3p$  XPS mea-

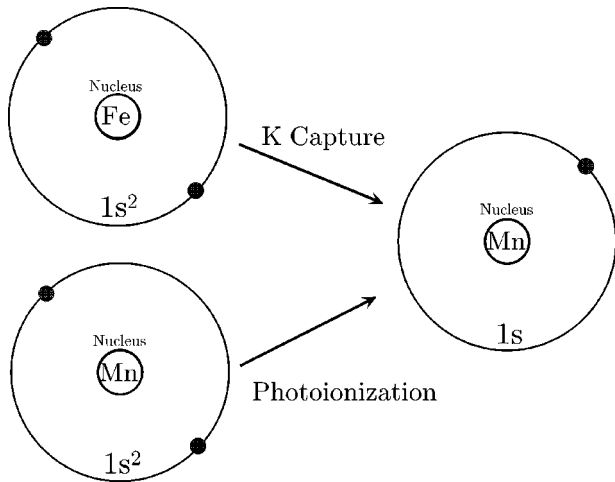


FIG. 1.  $K$  capture in  $^{55}\text{Fe}$  and  $1s$  photoionization in Mn. Both processes result in an ion that has a Mn ( $Z=25$ ) nucleus and a hole in the  $1s$  shell.

measurements and calculations for atomic Mn including, among other configurations,  $4s$  to  $3d$  shake-down processes, which can be considered the atomic equivalent to ligand-to-metal charge transfer in solids and molecules.<sup>15</sup> They distinguish between weak and strong CI depending on the overlap between the interacting electrons. The former can be approximated by appropriate scaling of the direct and exchange Slater integrals, while the latter requires explicit inclusion of the strongly interacting configurations. Mukoyama and Uda calculated the electron excitation probability due to the change of the central potential upon inner-shell vacancy creation, relating their results to shake-up probabilities.<sup>16</sup>

This paper intends to contribute to the discussion and to illuminate some aspects of the electronic relaxation after core electron excitation. We present a study of the radiative  $3p \rightarrow 1s$  ( $K\beta$ ) transition in MnO after photoionization (PI) and in  $^{55}\text{Fe}_2\text{O}_3$  after radioactive orbital electron capture decay from the  $K$  shell (KC). In both compounds, the metal is in an octahedral environment and has a  $3d^5$  valence electron configuration in the ionic approximation. The paper is organized as follows: First, a few remarks are made concerning electron-capture decay as an alternative mode of core hole creation compared to photoionization and some earlier  $K$  capture studies are summarized. The theoretical approach is outlined in Sec. II with emphasis on the treatment of the core hole effect depending on the mode of excitation. Experimental details are given in Sec. III and the calculations are described in Sec. IV. Theoretical and experimental results are compared in Sec. V.

### A. Orbital electron capture

Electron capture is a process closely related to nuclear  $\beta$  decay that competes with positron emission.<sup>17,18</sup> An orbital electron is captured by the nucleus yielding a neutron that remains in the nucleus and an escaping electron neutrino. The atomic number of the daughter nucleus is decreased by one while the atomic mass number is unchanged:  $Z^A + e^- \rightarrow (Z-1)^A + \nu_e$  (Fig. 1). The capture rate depends on the

probability of finding the electron inside the nucleus and is therefore largest for  $1s$  electrons.  $^{55}\text{Fe}$  decays into the nuclear ground state of  $^{55}\text{Mn}$ . Thus, only gamma emission due to the inner bremsstrahlung generated by the “falling” of the captured electron into the nucleus is emitted that does not measurably contribute to the background in the energy range of the x-ray emission following the decay of the resulting vacancy in the electron shell. The  $Q$  value of the electron capture decay of  $^{55}\text{Fe}$  is 231.6 keV (Ref. 19) and the recoil energy of the nucleus is calculated to 0.523 eV. Within the lifetime of the  $1s$  core hole ( $\sim 10^{-15}$  s) (Ref. 20) the distortion of the crystal lattice due to the nuclear recoil is not expected to have any influence on the  $K$  fluorescence spectra.

### B. Earlier $K$ capture studies

In a low-resolution experiment Hansen *et al.* measured the  $K$  fluorescence emission after  $K$  capture over an extended range in  $Z$  using Ge(Li) and Si(Li) detectors, respectively.<sup>21,22</sup> The  $K\beta/K\alpha$  ratio was found to be typical for the element in accordance with relativistic theoretical calculations by Scofield.<sup>23</sup> Hansen *et al.* obtained a better agreement with theory in KC experiments than earlier high-resolution PI experiments and explained the deviations in the PI studies with experimental difficulties. It was later pointed out by several authors that the  $K\beta/K\alpha$  ratio depends on the mode of excitation as well as on the chemical environment.<sup>24–29</sup> Mukoyama recently was able to explain the differences in V and Cr compounds theoretically by taking a higher M-shell shake-up and shake-off probability in PI than in KC into account.<sup>30</sup>

There are only few high-resolution studies of the  $K\beta$  emission in transition metals after  $K$  capture, presumably because a very strong radioactive source used to be necessary in order to obtain count rates sufficiently above the background noise. Schnopper *et al.* compared high-resolution  $K\beta$  spectra from a metallic 1 Ci  $^{55}\text{Fe}$  source with PI spectra of metallic Mn.<sup>31,32</sup> He discussed the probability of producing states of multiple excitation and ionization by readjustment after PI but within the experimental error he did not observe any differences in the spectra. Borchert *et al.* studied the x-ray emission in Au and Ho after  $K$  capture and after PI, and they observed relative shifts of the emission energies.<sup>33,34</sup> Dem'yanchuk *et al.* repeated the experiment on metallic  $^{55}\text{Fe}$  and reported a 0.6 eV shift of the  $K$  capture  $K\beta_{1,3}$  line relative to the x-ray excited line.<sup>35</sup> Recent results by the present authors in an improved experimental setup using a 5 mCi metallic  $^{55}\text{Fe}$  source showed in accordance with Schnopper that the  $K\beta$  main lines for both excitation modes occur at the same energy within the experimental error.<sup>36</sup> Furthermore, in the latter study the  $K\beta$  main line for metallic  $^{55}\text{Fe}$  after KC was found to be narrower than for metallic Mn after PI. In this paper, we propose a theoretical explanation for this narrowing in insulators but similar arguments can be applied to metals.

It shall be noted that changes in the nucleus (isotope effect, nuclear excitation) can influence the  $K$  fluorescence emission besides the mode of excitation and the chemical environment. Borchert *et al.* used  $K$  capture decay in

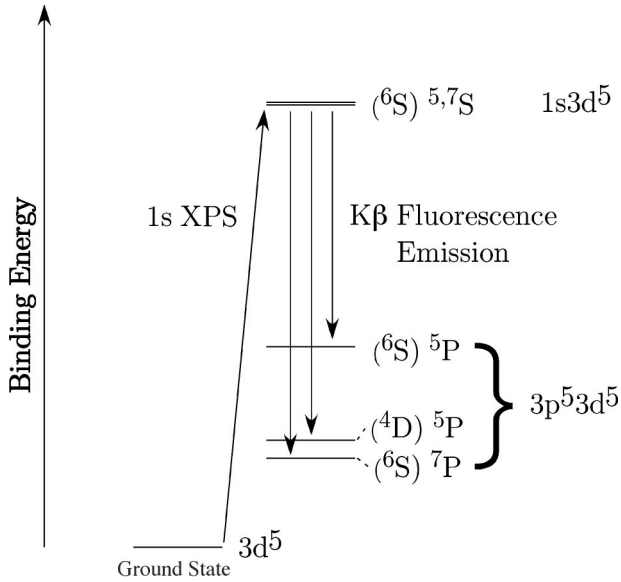


FIG. 2. Atomic term scheme for  $1s$  photoionization and  $K\beta$  fluorescence emission. The term in parenthesis denotes the  $3d$  parent term. Only the three final states with the strongest intensities are shown.

$^{131,132}\text{Cs}$  to observe shifts of the Xe  $K$  x-rays due to the nuclear finite-size effect and the magnetic hyperfine structure.<sup>37</sup> He pointed out that the expected shifts are on the order of  $10^{-2}$  to  $10^{-3}$  of the natural linewidth of the  $1s$  excited state. In the case of  $^{55}\text{Fe}$  this would result in a 1–10 meV shift, which is beyond the resolution of the crystal spectrometer employed in the studies presented here.

## II. THEORY

### A. Atomic multiplets and short range model

$K\beta$  fluorescence can be described as a two-step process as illustrated in Fig. 2 using atomic configurations. The  $1s$  intermediate state ( $1s3d^5$ ) is created either by photoionization or by a capture process. The  $1s$  hole is filled by a  $3p$  electron and the  $K\beta$  fluorescence lines are emitted. The final state has a hole in the  $3p$  shell ( $3p^53d^5$ ). The intermediate as well as the final state are split into sublevels due to spin-orbit and electron-electron Coulomb interaction. In an atomic picture, the ground state of  $\text{Mn}^{2+}$ , where only the  $3d$  shell is unfilled, has  $^6S$  symmetry and no spin-orbit splitting is present. In the intermediate state the  $1s$  hole ( $^2S$ ) couples to the  $3d$  electrons to give  $^5S$  and  $^7S$  terms separated by the ( $1s,3d$ ) exchange interaction. In the following these two states together will be addressed as the low-lying  $1s$  intermediate state. In the final state a  $3p$  hole ( $^2P$ ) couples to the  $3d$  electrons.

When a  $3p$  hole is created, nondiagonal electrostatic matrix elements can cause a spin flip in the  $3d$  shell giving a  $^4P$  and a  $^4D$  besides the  $^6S$   $3d$  parent term.<sup>15,38</sup> In atomic calculations, only the  $^4D$  term shows considerable intensity.<sup>15</sup> Together, with the dipole selection rules for optical transitions one obtains  $(^6S) ^5P$ ,  $(^6S) ^7P$ , and  $(^4D) ^5P$  for the final states, where the LS term in brackets refers to the sym-

metry in the  $3d$  shell. The  $(^6S) ^7P$  and  $(^6S) ^5P$  terms are split by the strong ( $3p,3d$ ) exchange interaction and spread over 15 eV. The ( $3d,3d$ ) direct interaction separates the  $(^6S) ^7P$  term from the  $(^4D) ^5P$  term. The  $(^6S) ^5P$  state is often referred to as the low-spin component because the unpaired spins of the  $3d$  shell are opposite in sign to the spin in the  $3p$  shell.

A cubic crystal field is introduced as a perturbation acting on the  $3d$  orbitals. The fivefold degeneracy is lowered to two distinct representations of  $T_{2g}$  and  $E_g$  symmetry. The two levels are separated by the cubic crystal field strength  $10 Dq$ . The  $S$  term of the ground state under  $SO_3$  symmetry transforms into  $A_{1g}$  in the octahedral symmetry  $O_h$  of the cubic crystal field. If  $Dq/B \leq 2.8$  where  $B$  is the Racah parameter [ $B = (9 * F_{dd}^2 - 5 * F_{dd}^4) / 441$ ] the ground state configuration is  $t_{2g}^3 e_g^2$  with  $^6A_{1g}$  symmetry as can be seen from the Tanabe-Sugano diagram.<sup>39</sup> It has been found theoretically and experimentally that the crystal-field strength only has a minor effect on the spectral shape of the  $K\beta$  emission as long as a high-spin configuration in the valence shell is maintained.<sup>40</sup>

So far, the model describing the  $K\beta$  fluorescence is an one-electron picture and electron correlation is only partly taken into account in the self-consistent field calculations by considering the Pauli exclusion principle. Hence, the mode of excitation (PI or KC) does not have any effect on the spectral shape. In the following approach, we treat electron correlation as configuration interaction in the framework of the short range or Anderson impurity model.<sup>41</sup> The metal  $d$  electrons are assumed to be localized at an energy  $\epsilon_d$  and the ligand  $p$  electrons delocalized in a band with mean energy  $\epsilon_p$ . Configuration interactions of the form  $|3d^5\rangle + |3d^6\bar{L}\rangle$ , where  $\bar{L}$  describes a ligand hole, are included in the calculations to account for ligand-to-metal charge-transfer. The charge-transfer energy  $\Delta$  that separates the centers of gravity of the multiplets of each configurations is defined as:  $\Delta = E(d^{n+1}\bar{L}) - E(d^n)$ .

The configurations  $3d^5$  and  $3d^6\bar{L}$  are mixed by a hopping term  $V$  that generates a bonding and antibonding combination. The hopping term  $V$  is dependent on the symmetry. In an octahedral surrounding two hopping terms exist,  $T(e_g)$  and  $T(t_{2g})$ , respectively, mixing  $E_g$  symmetry and  $T_{2g}$  symmetry ligand wave functions. The lowest-energy combination forms the true ground state that will be a linear combination of the form  $\alpha|3d^5\rangle + \beta|3d^6\bar{L}\rangle$ . From band structure calculations it is found that  $T(e_g)$  is approximately two times the value of  $T(t_{2g})$ .<sup>42</sup>

### B. Core hole effect

When a core hole is created upon photoionization the electrons adjust to the new potential. For  $3p$  and  $3d$  electrons the effective nuclear charge changes by approximately one.<sup>43</sup> The Hamiltonian describing the system relaxes from  $H_0$  in the ground state to  $H_1$  in the  $1s$  intermediate state during the time  $\tau_H$ . The relaxation time  $\tau_H$  is approximately two orders of magnitude shorter than the lifetime of the  $1s$  hole.<sup>44</sup> Relaxation can thus be treated as instantaneous for the  $K$  fluorescence decay.

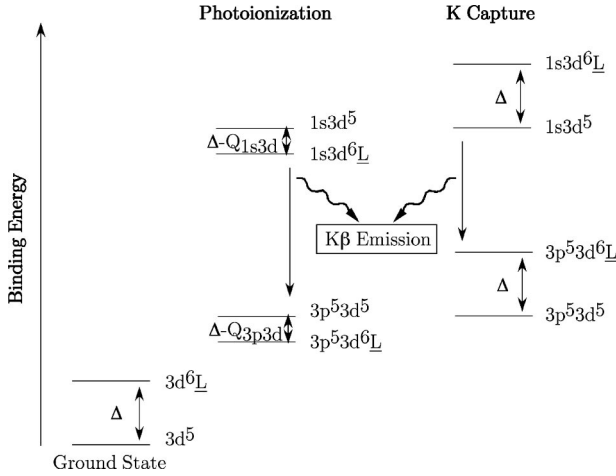


FIG. 3. Term scheme for the  $K\beta$  emission including two configurations. The ordering of the configurations changes after PI and remains unperturbed after KC.

Schnopper discussed the possibility of the outgoing electron perturbing the electron shell.<sup>32</sup> He concluded that this would cause a reversible deformation of the wave function of the bound electrons during the time of transit of the photoexcited electron through the orbital electron shell. Again, this would occur on a time scale much faster than the lifetime of the  $1s$  hole. We can therefore treat the final state of a  $1s$  photoionization as the fluorescence initial state for the  $K\beta$  emission if we assume that high-lying  $1s$  intermediate states do not decay to lower  $1s$  intermediate states before the  $1s$  vacancy is filled. This point will be addressed more detailed in Sec. V.

In the case of photoionization, the core-hole- $d$ -electron Coulomb attraction energy  $Q_{cd}$  changes the relative ordering of the  $1s3d^5$  and  $1s3d^6L$  configurations in the intermediate and in the final state (Fig. 3). The  $1s3d^6L$  charge transfer states are positioned below the  $1s3d^5$  states giving a change in the population of the two configurations when a core hole is created. It is interesting to note that Hansen calculated *ab initio* for Mn atoms that the  $3d^6(^5D)4s^6D$  term shifts below the  $3d^54s^2^6S$  term when a  $3p$  electron is removed.<sup>15</sup> This demonstrates the analogy between  $4s$  to  $3d$  shake-down processes in atoms and ligand-to-metal charge transfer in molecules and solids.

To illustrate the effect of this reordering we write the ground state as  $\phi_g = \sin(\alpha)|3d^5\rangle + \cos(\alpha)|3d^6L\rangle$ . The excited states are then  $\phi_{i1} = \sin(\beta)|3d^5\rangle + \cos(\beta)|3d^6L\rangle$  and  $\phi_{i2} = -\cos(\beta)|3d^5\rangle + \sin(\beta)|3d^6L\rangle$ . The intensity of the main peak is given as  $\cos^2(\beta - \alpha)$  and the satellite equals  $\sin^2(\beta - \alpha)$ . This implies that charge-transfer satellites occur when the two configurations reorder. No satellites occur when the population of the two configurations does not change.

The energy splitting between the bonding and the antibonding combination mainly depends on the hybridization and the splitting of the two configurations in the final state of the photoionization as will be shown in Sec. V.

Following Slater,<sup>43</sup> we assume that electrons from  $1s$  and  $3p$  orbitals screen one nuclear charge in the effective potential of  $3d$  electrons. When the  $1s$  electron is captured by the

nucleus (KC) and the  $1s$  vacancy is subsequently filled by a  $3p$  electron, the effective nuclear charge experienced by the  $3d$  electrons can be assumed to remain unchanged. The core-hole- $d$ -electron Coulomb attraction  $Q_{cd}$  is almost completely canceled by the decrease in the atomic number  $Z$ . Hence, the order of the configurations remains as it was in the ground state (Fig. 3) and only the lowest  $1s$  intermediate state is populated. The change of the core hole from  $1s$  to  $3p$  only has a small effect on  $Q_{cd}$  ( $\approx 0.5$  eV).<sup>45</sup> Calculations for several values of  $Q_{cd}$  show that this change can be neglected for the  $K\beta$  fluorescence. In Sec. V, it is shown how this reordering of the screened ( $1s3d^6L$ ) and unscreened ( $1s3d^5$ ) level effects the shape of the  $K\beta$  emission.

The  $1s$  intermediate state is reached from the ground state via the dipole operator in the photoionization experiment. A full treatment of the electron capture decay would involve the nuclear orbital electron capture decay transition operator that acts on the nucleus as well as on the electron shell. As described earlier, apart from the nuclear charge, we can neglect all changes in the nucleus. The effect of the electron capture transition operator on the electron shell is that it annihilates a  $1s$  electron. Assuming that in the KC process, the outer shells are not affected, the energy separation of the  $3d^5$  and  $3d^6L$  configuration does not change. The effect of the  $1s$  core hole on the electron shell is accounted for in the ligand field multiplet theory as described before. The intermediate states are split by the ( $1s, 3d$ ) exchange interaction and populated according to their statistical weight, i.e., 7:5 for the  $^7S$  and  $^5S$  final states, respectively.

### III. EXPERIMENTAL DETAILS

#### A. Sample preparation

The  $^{55}\text{Fe}$  was purchased from NEN Life Science products (Product # NEZ043) as Fe(III) in a 0.5M HCL solution with a specific activity of 45.3 mCi/mg.  $^{55}\text{Fe}_2\text{O}_3$  was prepared by first spiking 0.05 mL of  $^{55}\text{Fe}$  ferric nitrate solution into 13.6 mg stable reagent grade  $\text{Fe}(\text{NO}_3)_3 \cdot 9\text{H}_2\text{O}$  dissolved in 1-mL  $\text{H}_2\text{O}$ .  $\text{NH}_4\text{OH}$  (2M) was then added dropwise to complete the  $\text{Fe}(\text{OH})_3$  precipitation. The  $\text{Fe}(\text{OH})_3$  precipitate was centrifuged, washed twice with 2 mL  $\text{H}_2\text{O}$ , dried under a heat lamp, and heated further to cause transformation to  $\text{Fe}_2\text{O}_3$ . The resulting material was loaded into a  $5 \times 1 \times 1$  mm<sup>3</sup> groove of a small aluminum plate. In order to seal the radioactive material the sample holders were wrapped in Kapton foil. The measured activity of the sample was  $\approx 0.5$  mCi.

MnO (99.5%) was used as received from Alfa/AESAR. For the x-ray emission measurements, the MnO was loaded into a similar aluminum sample holder and wrapped in Kapton foil. During the PI measurement, the MnO sample was kept at room temperature. In previous experiments, we observed no significant radiation damage in MnO, and thus, sample cooling was not necessary.

#### B. Fluorescence experiment

The x-ray excited  $K\beta$  spectra were taken on the wiggler beamline 10-2 at the Stanford Synchrotron Radiation Laboratory. The synchrotron radiation was monochromated using

a pair of Si(111) crystals and focused onto the sample with a cylindrical mirror. The incident photon flux was recorded with an  $N_2$  filled ion chamber. The excitation energy was set at 9140 eV, well above the Mn  $K$  edge in order to avoid post-collision interaction (PCI) effects. At this energy, the incident flux was on the order of  $10^{11}$  photons/sec.

For both the x-ray excited, as well as the  $K$  capture measurements, the same multicrystal array spectrometer was employed to measure the  $K\beta$  emission. The spectra are recorded in a backscattering geometry using the Si(440) Bragg reflection from eight spherically bent crystals arranged in a Rowland geometry with the Rowland circle lying in a vertical plane. A Ge detector centered in the common focus of the eight crystals measures the fluorescence intensity. A He bag encloses the entire emitted beam path. In order to minimize the background (primarily from elastic scattering) lead shielding is used around the sample and a 3\*15 mm lead slit is placed in front of the detector. The Ge detector is used to window out inelastically scattered x rays and so to improve the signal to noise ratio. A detailed description of the instrument is available.<sup>46</sup>

Absolute energy calibration of the spectrometer is achieved by measuring the angle between the sample and the center of the crystals and using the known  $d$  spacing for Si (5.4309 Å) with Bragg's law. We give an upper limit for the error of the absolute energy calibration to 1 eV.

For comparison of the two different spectroscopic techniques ( $K$  capture and photoionization), relative energy calibration, as well as constant energy resolution, are crucial aspects of the experimental procedure. For the x-ray excited measurements, a well-defined excitation beam was obtained by placing a 1 mm vertical by 2 mm horizontal slit in front of the samples. An ion chamber filled with  $N_2$  was placed behind the slit to measure the incoming photon flux. The entire experimental apparatus could be adjusted vertically in order to compensate for vertical movements of the synchrotron beam and thus maintain the energy calibration. To switch from the x-ray excited to the  $K$  capture measurement, the synchrotron beam position on the sample was first determined, defining the source volume of the spectrometer. The radioactive source was then placed into the source volume with an estimated vertical accuracy of 0.2 mm. This translates into an error for the relative energy calibration of 0.15 eV.

The overall energy resolution of the spectrometer can be separated into an intrinsic band-width  $\Delta E_{int}$  of the crystals and geometrical contributions  $\Delta E_{geo}$  that depend on the experimental setup.  $\Delta E_{int}$  is the same for the x ray and the  $K$  capture measurements because the same crystals were used.  $\Delta E_{geo}$  is mainly determined by the horizontal and vertical dimensions of the emitting sample surface. As mentioned above the surface of the radioactive sample was 1 mm high by 5 mm wide. For the synchrotron experiment the 1 mm by 2 mm excitation beam hit the sample at an angle of  $25^\circ$  relative to the normal on the sample surface giving an emitting surface 1 mm high and approximately 5 mm wide. Thus, the resulting energy bandwidth of the fluorescence spectrometer was  $\approx 0.7$  eV for both the x-ray excited as well as the  $K$  capture experiment.

TABLE I. Parameters used in the charge-transfer calculations. For all configurations  $V(e_g)$  was set to 2.0.  $V(t_{2g})$  is half this value. For each state, the separation of the two configurations ( $\Delta$  or  $\Delta - Q_{cd}$ ) is given in the third column. All configurational parameters are given in (eV) units.

Ground State	$3d^5$	$\Delta = 7.0^a$ $\Delta = 3.5^b$	$3d^6\bar{L}$
	$\zeta_d = 0.04$		$\zeta_d = 0.04$
	$F_{dd}^2 = 10.32$		$F_{dd}^2 = 9.07$
	$F_{dd}^4 = 6.41$		$F_{dd}^4 = 5.59$
Intermediate State	$1s3d^5$	$\Delta - Q_{1s3d} = -2^a$ $\Delta = 3.5^b$	$1s3d^6\bar{L}$
	$\zeta_d = 0.06$		$\zeta_d = 0.05$
	$F_{dd}^2 = 12.12$		$F_{dd}^2 = 11.05$
	$F_{dd}^4 = 7.58$		$F_{dd}^4 = 6.87$
	$G_{sd}^2 = 0.06$		$G_{sd}^2 = 0.05$
Final State	$3p^53d^5$	$\Delta - Q_{3p3d} = -2^a$ $\Delta = 3.5^b$	$3p^53d^6\bar{L}$
	$\zeta_d = 0.05$		$\zeta_d = 0.04$
	$\zeta_p = 0.80$		$\zeta_p = 0.77$
	$F_{dd}^2 = 11.47$		$F_{dd}^2 = 10.43$
	$F_{dd}^4 = 7.18$		$F_{dd}^4 = 6.49$
	$F_{pd}^2 = 12.40$		$F_{pd}^2 = 11.64$
	$G_{pd}^1 = 15.40$		$G_{pd}^1 = 14.50$
	$G_{pd}^3 = 9.38$		$G_{pd}^3 = 8.75$

<sup>a</sup>PI in MnO.

<sup>b</sup>KC in Fe<sub>2</sub>O<sub>3</sub>.

To avoid detector pileup effects, the count rate detected by the Ge detector at the strongest fluorescence peak ( $K\beta_{1,3}$ ) was maintained at  $\approx 20\,000$  cts/s in the x-ray excited measurements by placing an aluminum filter in the SR beam path. The 0.5 mCi radioactive sample yielded 10 cts/s in the main peak.

## IV. CALCULATIONS

### A. Crystal-field multiplet calculations

The single-configuration electron-electron Coulomb integrals (Slater integrals) and the spin-orbit parameters were calculated within the Hartree-Fock limit using the code developed by Cowan.<sup>7</sup> The results are summarized in Table I together with the values used for the charge-transfer energy  $\Delta$  and the core-hole- $d$ -electron attraction  $Q_{cd}$ . For the  $3p^53d^5$  ( $3p^53d^6\bar{L}$ ) final-state configuration the  $F_{dd}^2$ ,  $F_{dd}^4$  and  $F_{pd}^2$  direct and the  $G_{pd}^1$  and  $G_{pd}^3$  exchange integrals were calculated as well as the  $\zeta_{3p}$  spin-orbit coupling. The Coulomb integrals  $F_{pd}$  and  $G_{pd}$  were scaled down to 70% of their single configuration values in order to account for intra-atomic configuration interaction effects.<sup>7</sup> The scaling was set such that the  $K\beta_{1,3}$ - $K\beta'$  separation observed in the  $K$  capture experiment was approximately reproduced in the calculated spectrum. The same scaling was then used for the PI and the KC calculations. For the calculation of the  $1s$  intermediate states, the  $1s3d^5\epsilon p$  and  $1s3d^6\bar{L}\epsilon p$  channels were

taken into account and no interaction of the continuum electron with the ionized atom was considered.

The measured values for the crystal-field splitting given in the literature are 0.8 eV for MnO and 1.45 eV for Fe<sub>2</sub>O<sub>3</sub>, respectively.<sup>2,47</sup> In order to compare MnO and Fe<sub>2</sub>O<sub>3</sub> directly we used a common value of 1.0 eV in the calculations. The use of the published values for MnO and Fe<sub>2</sub>O<sub>3</sub> will not visibly affect the spectral shape.

For the charge-transfer energy  $\Delta$  and the core-hole- $d$ -electron Coulomb attraction  $Q_{cd}$  we followed the results of Bocquet for  $2p$  XPS (Ref. 48) and used  $\Delta=7.0$  eV and  $Q_{cd}=9.0$  eV for MnO and  $\Delta=3.5$  for Fe<sub>2</sub>O<sub>3</sub> (no  $Q_{cd}$  value was used for Fe<sub>2</sub>O<sub>3</sub>).  $Q_{1s3d}$  was set equal to  $Q_{3p3d}$ . The hopping term  $T$  was set for both compounds to 2.0 eV for the  $e_g$  orbitals and to 1.0 eV for the  $t_{2g}$  orbitals. The  $E_g$  hopping term identifies with the  $pd\sigma$  hybridization and the  $T_{2g}$  hopping term with the  $pd\pi$  hybridization.

For the PI, as well as the KC calculations, the same total energy for the final-state configuration was assumed, i.e., the ‘‘center of mass’’ of the multiplet is identical in both cases.

### B. Lifetime broadening

For an accurate treatment of the lifetime broadening, one has to include the lifetime of the final state besides the lifetime of the  $1s$  intermediate state. The final states mainly decay non-radiatively via a Coster-Kronig (CK) or a super-Coster-Kronig decay (sCK).<sup>12</sup> Calculations by several authors showed that the decay rates strongly depend on the multiplet term of the final state and they could successfully explain the suppression of the low-spin components in the  $3p$  XPS of atomic Cr and Mn and in the  $K\beta$  spectra of Mn compounds.<sup>12,15</sup> For the latter, satisfactory agreement was achieved for MnO and MnF<sub>2</sub> between theory and experiment by assuming a linear relation (0.2 $\omega$  FWHM) between the final-state energy and the lifetime broadening of the final states. Hansen *et al.* obtained 0.13 eV and 2.5 eV FWHM including CI for the  $3p^53d^5(^6S)$   $^7P$  and  $^5P$  final states of atomic Mn, respectively.<sup>15</sup> They found a considerable decrease in the final state lifetime in CI calculations over single-configuration calculations for Mn atoms.

From Fig. 3, one can expect that the final-state lifetime broadening is different for KC than for PI. The core-hole- $d$ -potential pulls the configurations closer together and inverts the order of the two configurations suggesting stronger CI for PI than for KC. The charge-transfer calculations give 85.4%  $3d^5$  and 14.6%  $3d^6L$  for KC and 42.1%  $3d^5$  and 57.9%  $3d^6L$  for PI. Furthermore, a sCK decay is forbidden for the septet of a  $3p^53d^5$  configuration, while it is allowed for a  $3p^53d^6L$  configuration. Considering these qualitative arguments we discuss in Sec. V whether a different final-state lifetime broadening has to be taken into account in order to explain the experimental results.

## V. RESULTS AND DISCUSSION

The experimental  $K\beta$  spectra of MnO after x-ray excitation and <sup>55</sup>Fe<sub>2</sub>O<sub>3</sub> following  $K$  capture are compared in Fig.

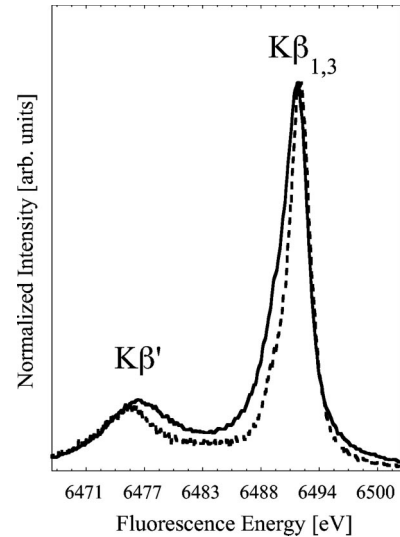


FIG. 4. Experimental  $K\beta$  spectra for MnO (solid line) and <sup>55</sup>Fe<sub>2</sub>O<sub>3</sub> (dashed line). The instrumental broadening is  $\approx 0.7$  eV.

4. The energy range of the  $3p$  to  $1s$  transitions is shown with the sharp  $K\beta_{1,3}$  peak at higher-fluorescence energies and a broad  $K\beta'$  structure at lower-fluorescence energies. The spectral intensities have been normalized to each other in the maximum of the  $K\beta_{1,3}$  peak. The energy scale is the measured fluorescence energy and the spectra were not shifted in energy with respect to each other. A constant background was subtracted from the KC spectrum but not from the PI spectrum because of the very good signal to background ratio in the latter case.

The two spectra nearly coincide on the low-energy side of the  $K\beta'$  structure. The  $K\beta'$  peak is slightly weaker and shifted to lower energies for <sup>55</sup>Fe<sub>2</sub>O<sub>3</sub>, and the MnO PI spectrum shows considerably more intensity between  $K\beta'$  and  $K\beta_{1,3}$ . The  $K\beta_{1,3}$  peak appears sharper for KC and shifted to higher-fluorescence energies. Furthermore, the MnO PI spectrum shows more intensity in the high-energy tail of the  $K\beta_{1,3}$  line.

The calculated  $1s$  intermediate states for MnO after PI and <sup>55</sup>Fe<sub>2</sub>O<sub>3</sub> following KC are shown in Fig. 5. The solid curves are obtained by convoluting the line spectra with a Lorentzian function (1.16 eV FWHM) reflecting the lifetime of the  $1s$  hole.<sup>20</sup> Two final states split by the weak ( $1s,3d$ ) exchange interaction and populated according to their statistical weight are reached after the KC decay that merge into one peak due to lifetime broadening. This peak corresponds to the  $1s$  intermediate state bonding configuration. The antibonding combination is not populated because the ordering of the  $3d^5$  and  $3d^6L$  is assumed to remain unchanged.

Two strong features separated by  $\approx 6.8$  eV appear in the  $1s$  intermediate states after PI. The core-hole potential gives a reordering of the levels with the  $1s3d^6L$  configuration 2 eV below the  $1s3d^5$  configuration. This reordering transfers intensity to the antibonding combination that appears as a satellite at higher-binding energies. To illustrate the influence of the charge-transfer energy  $\Delta$  and the hopping term  $V$  on the splitting between the bonding and the antibonding combination, we calculated the splitting for different param-

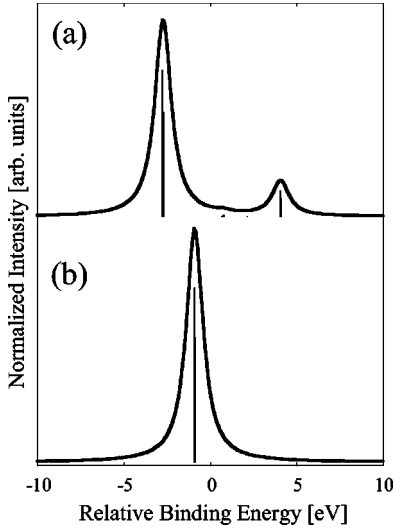


FIG. 5. Calculated  $1s$  intermediate states for (a) PI and (b) KC. A  $1s$  XPS charge-transfer calculation was performed for PI. The intermediate states after KC are reached via annihilation of a  $1s$  electron. The two configurations reorder in (a) due to the core-hole effect while the ground-state splitting is maintained in (b). The stick spectra are convoluted with a 1.16 FWHM Lorentzian to account for the  $1s$  lifetime.

eters. For  $T(e_g)=1.0$  eV and  $T(t_{2g})=0.5$  eV the splitting is reduced to 3.6 eV while an increase of the separation of the two configurations ( $\Delta$ ) from 2 eV to 8 eV results in an increase to 8.3 eV of the bonding-antibonding splitting.

In the following, we will refer to the two strong features as the low- and the high-lying  $1s$  intermediate state, respectively. Other weakly populated intermediate states can be neglected for the present discussion.

The calculated  $K\beta$  spectra are shown in Fig. 6. The energy scale is shifted to coincide with the experimental fluorescence energies. The  $^{55}\text{Fe}_2\text{O}_3$  KC spectrum was calculated using the one populated  $1s$  intermediate state while for the MnO PI spectrum, two  $K\beta$  spectra were calculated corresponding to the two strongly populated  $1s$  intermediate states. All spectra were convoluted with a 1.16 eV FWHM Lorentzian to account for the  $1s$  lifetime broadening and a 0.7 eV FWHM Gaussian for the instrumental broadening. To account for the term-dependent final-state lifetime broadening we followed the procedure suggested by Taguchi *et al.*<sup>12</sup> and assumed a linear increase of the final-state lifetime broadening towards lower-fluorescence energies ( $-0.2\omega$  FWHM). We chose 0.4 eV as the starting value for this linear increase at the final state with highest-fluorescence energy. This value is motivated by the value for atoms (0.13 eV) assuming shorter lifetime in the solid. The final-state lifetime broadening applied to the spectra is shown in Fig. 6(d).

The shoulder on the low-energy side of the  $K\beta_{1,3}$  peak in the  $^{55}\text{Fe}_2\text{O}_3$  KC spectrum is due to a multiplet term with a recoupled  $3d$  shell. The calculated spectrum for PI in MnO shows that the intensity in the recoupled term is reduced as a result of the core-hole- $d$ -electron potential and the inclusion

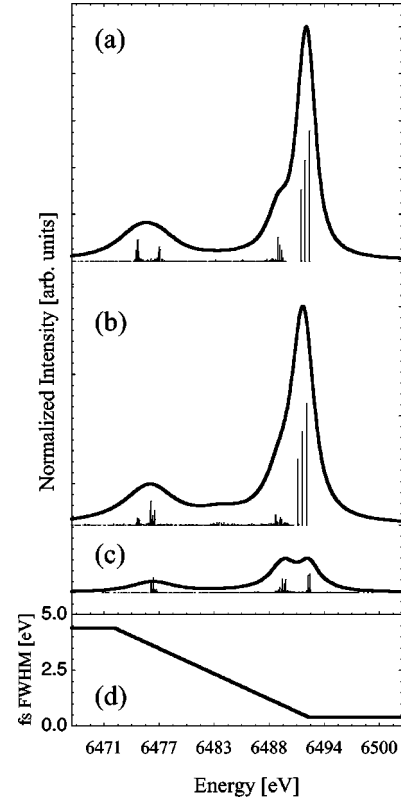


FIG. 6. Calculated  $K\beta$  spectra for (a) KC in  $^{55}\text{Fe}_2\text{O}_3$  and (b),(c) for MnO after PI. For the latter, part (b) shows the spectrum resulting from the low-lying  $1s$  intermediate state, while (c) shows the spectrum resulting from the high-lying  $1s$  intermediate state. The final state ( $fs$ ) lifetime broadening applied to the spectra is given in (d).

of charge transfer because the  $3d^6\bar{L}$  configuration shifts below the  $3d^5$  configuration.

The splitting between  $K\beta_{1,3}$  and  $K\beta'$  is due to the  $(3p,3d)$  exchange interaction as described in Sec. II. The splitting appears reduced in the PI experiment compared to the KC data. The magnitude of the splitting depends on the number of unpaired spins in the  $3d$  shell. The final states after PI have a stronger  $3d^6\bar{L}$  admixture than the final states after KC. This means that the net spin in the  $3d$  shell is reduced due to the core-hole effect in PI and the splitting between  $K\beta_{1,3}$  and  $K\beta'$  is smaller in PI than after KC. Besides this real reduction of the exchange splitting, there is an apparent reduction of the splitting of the two peaks because of additional final states between the two peaks that are populated after PI (Fig. 6).

In order to quantify the results, we reduced the spectra to their 1st ( $M_1$ ), 2nd ( $M_2$ ), and 3rd moments ( $M_3$ ) defined as  $M_1 = \sum c_i e_i / \sum c_i$ ,  $M_2 = \sum c_i (M_1 - e_i)^2 / \sum c_i$ , and  $M_3 = \sum c_i (M_1 - e_i)^3 / \sum c_i$  where  $c_i$  is the count rate at energy  $e_i$ . An energy range has to be picked for the moment calculations. We chose the energies at 50% of the maximum  $K\beta_{1,3}$  intensity as the upper and lower limit for the energy range. For the  $K\beta_{1,3}$  peak all three moments were calculated. For  $K\beta'$  only the first moment ( $M_1'$ ) was calculated using an energy range that includes intensities down to 70% of the

TABLE II. Experimental and calculated moments for MnO and  $^{55}\text{Fe}_2\text{O}_3$ . Four sets are given for MnO after PI. In (a) and (b), the same final-state lifetime broadening as for  $^{55}\text{Fe}_2\text{O}_3$  after KC was applied. Only the low-lying  $1s$  intermediate state is included in (a), while in (b), both  $1s$  intermediate states are included. In (c) and (d), a greater final-state lifetime broadening was applied. In (c), only the low-lying  $1s$  intermediate state is included, while in (d), both  $1s$  intermediate states are included. The statistical errors are smaller than the accuracy given in the Table. The error for  $M_1$  in MnO is due to the experimental uncertainty for the relative energy calibration.

	$M_1^a$ [eV]	$M_2$ [ $10^{-1} (\text{eV})^2$ ]	$M_3$ [ $10^{-1} (\text{eV})^3$ ]	$M_1-M_1'$ [eV]
<b>Experiment</b>				
$^{55}\text{Fe}_2\text{O}_3$	0	4.33	-0.13	16.50
MnO	-0.56(15)	8.69	-1.35	14.80
<b>Theory</b>				
$^{55}\text{Fe}_2\text{O}_3$	0 <sup>b</sup>	3.89	-0.11	16.34
MnO				
(a)	-0.31 <sup>b</sup>	4.23	-0.18	15.63
(b)	-0.37 <sup>b</sup>	5.42	-0.49	15.50
(c)	-0.40 <sup>b</sup>	6.56	-0.47	15.50
(d)	-0.51 <sup>b</sup>	8.72	-1.20	15.31

<sup>a</sup>- 6492.08 eV.

<sup>b</sup>Shifted such that  $M_1$  of theoretical  $^{55}\text{Fe}_2\text{O}_3$  spectrum coincides with experiment.

$K\beta'$  peak intensity. The first moment can be interpreted as the ‘‘center of mass,’’ while the second moment is related to the width and the third moment to the asymmetry of the spectral feature.

The results for the experimental as well as the theoretical spectra are summarized in Table II. The energy scale for the theoretical spectra was shifted such that  $M_1$  for  $^{55}\text{Fe}_2\text{O}_3$  coincides with the experimental value. The other parameters in Table II are not effected by this shift. The first moment for  $K\beta'$  was used to determine the difference  $M_1-M_1'$  between  $K\beta_{1,3}$  and  $K\beta'$ . The statistical errors have been calculated for the experimental spectra and found to be negligible within the accuracy given in Table II. Hence, only for  $M_1$ , an error is given due to the uncertainty in the relative energy calibration.

The experimental values in Table II confirm the results from a visual inspection of the spectra:  $M_1$  is shifted to lower energies for MnO PI,  $M_2$  is about twice as large and  $M_3$  for MnO PI is about ten times as large as the corresponding values for  $^{55}\text{Fe}_2\text{O}_3$  KC. The difference  $M_1-M_1'$  is by 1.7 eV smaller for MnO PI.

The good agreement of the theoretical values for  $^{55}\text{Fe}_2\text{O}_3$  KC for  $M_2$  and  $M_1-M_1'$  with the experiment is due to the adjustment of the parameters for the final-state lifetime

broadening and the scaling of the Coulomb integrals. The asymmetry  $M_3$  is well reproduced in the theoretical spectrum.

Four different cases for the MnO PI calculations are considered. The parameters in (a) only include the lowest  $1s$  intermediate state. This case already reproduces the correct trend for all parameters.  $M_1$  is shifted to lower energies,  $K\beta_{1,3}$  and  $K\beta'$  move closer together ( $M_1-M_1'$ ) and the spectrum is broader and more asymmetric than for KC. The parameters in (b) were obtained from the MnO  $K\beta$  spectrum that includes both strong  $1s$  intermediate states. The high-lying  $1s$  intermediate state broadens the spectrum on the low energy side resulting in a considerable increase for  $M_3$ . The agreement with experiment is better for all parameters. In (a) and (b), we assumed the same final-state lifetime broadening for KC and PI.

In order to investigate the influence of the final-state lifetime broadening, we determined the moments for a different broadening in MnO PI. In Table II (c) and (d) we assumed 0.9 eV FWHM instead of 0.4 eV FWHM at high fluorescence energies and assumed the same linear increase of the broadening with decreasing fluorescence energy ( $-0.2\omega$  FWHM). The results for the moments including only the lowest  $1s$  intermediate state are shown in Table II (c). The

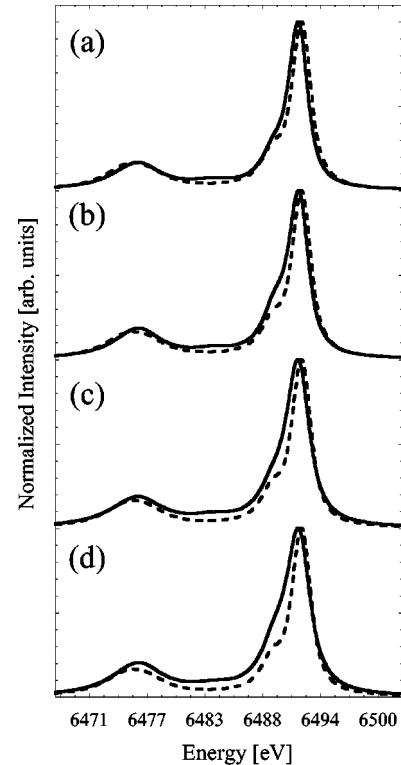


FIG. 7. Calculated  $K\beta$  spectra after PI in MnO (solid lines) and KC in  $^{55}\text{Fe}_2\text{O}_3$  (dashed lines). The KC spectra are the same in all four cases while four different MnO PI spectra are shown. In (a) and (b) the same final-state lifetime broadening was applied. Only the low-lying  $1s$  intermediate state is included in (a), while in (b), both  $1s$  intermediate states are included. In (c) and (d), a greater final-state lifetime broadening was applied. In (c), only the low-lying  $1s$  intermediate state is included, while in (d), both  $1s$  intermediate states are included.

agreement between experiment and theory is improved for all parameters compared to case (a) with equal final-state lifetimes for KC and PI.

At this point, it is tempting to further increase the final-state lifetime broadening in order to further improve the agreement with experiment. However, it is not possible to achieve good agreement for  $M_2$  and  $M_3$  simultaneously. A final-state lifetime that would bring  $M_2$  of the theoretical spectrum to match with the experimental spectrum would result in a strong deviation between theory and experiment for  $M_3$ .

In Table II (d) the same lifetime broadening as in (c) was used, but now the high-lying  $1s$  intermediate state was included for the calculation of the  $K\beta$  spectrum.  $M_1$ ,  $M_2$ , and  $M_3$  are now very close to the experimental values while ( $M_1 - M_1'$ ) is still off by 0.51 eV. This case gives the best agreement between theory and experiment for all four parameters.

The spectra corresponding to the four cases (a)–(d) are shown in Fig. 7. The different MnO PI spectra are compared to the same  $^{55}\text{Fe}_2\text{O}_3$  KC spectrum. The experimental results from Fig. 4 are best reproduced for case (d). We therefore conclude that both effects, high-lying  $1s$  excited states, as well as different final-state lifetime broadening, have to be taken into account in order to explain the differences between KC and PI.

An alternative approach to explain the differences between KC and PI would be to calculate the intensities and fluorescence energies for states with shake-off configurations. Measurements by the present authors of  $KL\beta$  ( $L$ -shake-off) lines suggest that the fluorescence energies for shake-off transitions can be estimated using a simple  $Z+1$  model. This model yields higher-fluorescence energies for the shake-off lines than for the  $K\beta$  lines. Thus, shake-off transitions would result in a broadening on the high-energy

side of the  $K\beta_{1,3}$  in contradiction to the experimental observation.

## VI. CONCLUSION

The influence of the core hole on the  $K\beta$  emission in MnO and  $^{55}\text{Fe}_2\text{O}_3$  was investigated by comparison of two different modes of excitation. The differences between the spectra can be understood in the framework of a ligand field multiplet model including ligand-to-metal charge transfer. The core-hole-d-electron potential causes a reordering of the configurations after photoionization. This reordering does not occur after  $K$  capture decay.

The calculations show that high-lying  $1s$  intermediate states are populated after PI. Best agreement between theory and experiment is achieved by including the high-lying  $1s$  intermediate state as fluorescence initial state for the  $K\beta$  transition as well as assuming an increased final-state lifetime broadening after PI.

We showed that comparison of two modes of excitation is a valuable method to investigate the effect of the core hole. The differences cannot be explained in a single-electron picture. Comparison of the two spectroscopic techniques therefore offers a tool to evaluate the effect of electron correlation in solids.

## ACKNOWLEDGMENTS

We thank Sandra Fiskum at PNNL for preparing the  $^{55}\text{Fe}_2\text{O}_3$  sample. We thank Hal Tompkins and the beamline 10-2 staff at SSRL for assistance in making these experiments possible. SSRL is funded by the Department of Energy, Office of Basic Energy Sciences. We are indebted to Jorgen Hansen for fruitful discussions. This work was supported by the National Institutes of Health GM-44380 and the Department of Energy, Office of Biological, and Environmental Research.

<sup>1</sup>A. Meisel, G. Leonhardt, and R. Szargan, in *X-Ray Spectra and Chemical Binding*, Chemical Physics Vol. 37, edited by F.P. Schafer, V.I. Goldanskii, and J.P. Toennies (Springer-Verlag, Berlin, 1989).

<sup>2</sup>F. de Groot, J. Electron Spectrosc. Relat. Phenom. **676**, 529 (1994).

<sup>3</sup>*New Directions in Research with Third-Generation Soft X-ray Synchrotron Radiation Sources*, Applied Sciences Vol. 254, edited by A.S. Schlachter and F.J. Wuilleumier (Kluwer Academic, Dordrecht, 1994).

<sup>4</sup>T.A. Tyson, Q. Qian, C.C. Kao, J.P. Rueff, F.M.F. de Groot, M. Croft, S.W. Cheong, M. Greenblatt, and M.A. Subramanian, Phys. Rev. B **60**, 4665 (1999).

<sup>5</sup>Y. Tokura and N. Nagaosa, Science **288**, 462 (2000).

<sup>6</sup>U. Bergmann, M.M. Grush, C.R. Horne, P. DeMarois, J.E. Penner-Hahn, C.F. Yocum, D.W. Wright, C.E. Dube, W.H. Armstrong, G. Christou, H.J. Eppley, and S.P. Cramer, J. Phys. Chem. B **102**, 8350 (1998).

<sup>7</sup>R.D. Cowan, *The Theory of Atomic Structure and Spectra* (University of California Press, Berkeley, 1981).

<sup>8</sup>J. Fink, T. Muller-Heinzerling, B. Scheerer, W. Speier, F.U. Hillbrecht, J.C. Fuggle, J. Zaanen, and G.A. Sawatzky, Phys. Rev. B **32**, 4899 (1985).

<sup>9</sup>G. van der Laan, J. Zaanen, G.A. Sawatzky, A. Karnatak, and J.M. Esteve, Solid State Commun. **56**, 673 (1985).

<sup>10</sup>J. Zaanen, C. Westra, and G.A. Sawatzky, Phys. Rev. B **33**, 8060 (1986).

<sup>11</sup>J. Park, S. Ryu, M. Han, and S.J. Oh, Phys. Rev. B **37**, 10 867 (1988).

<sup>12</sup>M. Taguchi, T. Uozumi, and A. Kotani, J. Phys. Soc. Jpn. **66**, 247 (1997).

<sup>13</sup>M. Taguchi, J.C. Parlebas, T. Uozumi, A. Kotani, and C.C. Kao, Phys. Rev. B **61**, 2553 (2000).

<sup>14</sup>J. Kawai, C. Suzuki, H. Adachi, T. Konishi, and Y. Gohshi, Phys. Rev. B **50**, 11 347 (1994).

<sup>15</sup>A. Von dem Borne, R.L. Johnson, B. Sonntag, M. Talkenberg, A. Verwey, Ph. Wernet, J. Schulz, K. Tiedtke, C. Gerth, B. Obst, P. Zimmermann, and J.E. Hansen, Phys. Rev. A **62**, 052703 (2000).

<sup>16</sup>T. Mukoyama and M. Uda, Phys. Rev. A **61**, 030501 (2000).

- <sup>17</sup>E.J. Konopinski, in *The Theory of Beta Radioactivity, The International Series of Monographs in Physics*, edited by N.F. Mott, E.C. Bullard, and D.H. Wilkinson (Oxford University Press, London, 1966).
- <sup>18</sup>C.S. Wu and S.A. Moszkowski, in *Beta Decay, Interscience Monographs and Texts in Physics and Astronomy*, Vol. 16, edited by R.E. Marshak (Interscience Publishers, New York, 1966).
- <sup>19</sup>*Handbook of Chemistry and Physics*, edited by D.R. Lide (CRC Press, Boca Raton, 1996–1997), 7th ed.
- <sup>20</sup>M.O. Krause and J.H. Oliver, *J. Phys. Chem. Ref. Data* **8**, 329 (1979).
- <sup>21</sup>J.S. Hansen, H.U. Freund, and R.W. Fink, *Nucl. Phys. A* **142**, 604 (1970).
- <sup>22</sup>J.S. Hansen, H.U. Freund, and R.W. Fink, *Nucl. Phys. A* **153**, 465 (1970).
- <sup>23</sup>J.H. Scofield, *Phys. Rev.* **179**, 9 (1969).
- <sup>24</sup>E. Bykkasap, A. Kcknder, Z. Sahin, and H. Erdogan, *J. Radioanal. Nucl. Chem.* **186**, 471 (1994).
- <sup>25</sup>N. Venkateswara Rao, S. Bhuloka Reddy, and D.L. Sastry, *Nuovo Cimento A* **97**, 1 (1987).
- <sup>26</sup>G. Paic and V. Pecar, *Phys. Rev. A* **14**, 2190 (1976).
- <sup>27</sup>S. Raj, H.C. Padhi, and M. Polasik, *Nucl. Instrum. Methods Phys. Res. B* **145**, 485 (1998).
- <sup>28</sup>S. Raj, H.C. Padhi, and M. Polasik, *Nucl. Instrum. Methods Phys. Res. B* **160**, 443 (2000).
- <sup>29</sup>K.C. Wang, A.A. Hahn, F. Boehm, and P. Vogel, *Phys. Rev. A* **18**, 2580 (1978).
- <sup>30</sup>T. Mukoyama and K. Taniguchi, *Adv. Quantum Chem.* **37**, 139 (2000).
- <sup>31</sup>H.W. Schnopper, *Phys. Rev.* **131**, 2558 (1963).
- <sup>32</sup>H.W. Schnopper, *Phys. Rev.* **154**, 118 (1967).
- <sup>33</sup>G.L. Borchert, P.G. Hansen, B. Johnson, I. Lindgren, H.L. Ravn, O.W.B. Schult, and P. Tidemand-Petersson, *Phys. Lett. A* **66A**, 374 (1978).
- <sup>34</sup>G.L. Borchert, P.G. Hansen, B. Johnson, I. Lindgren, H.L. Ravn, O.W.B. Schult, and P. Tidemand-Petersson, *Phys. Lett. A* **65A**, 297 (1978).
- <sup>35</sup>A.V. Dem'yanchuk, A.Z. Zhmudskiy, V.F. Surzhko, and V.I. Shiyonovskiy, *Fiz. Met. Metalloved.* **43**, 1307 (1977).
- <sup>36</sup>U. Bergmann, P. Glatzel, F. deGroot, and S.P. Cramer, *J. Am. Chem. Soc.* **121**, 4926 (1999).
- <sup>37</sup>G.L. Borchert, P.G. Hansen, B. Johnson, H.L. Ravn, O.W.B. Schult, and P. Tidemand-Petersson, *Phys. Lett. A* **63A**, 15 (1977).
- <sup>38</sup>F.M.F. de Groot, A. Fontaine, C.C. Kao, and M. Krisch, *J. Phys. A* **6**, 6875 (1994).
- <sup>39</sup>S. Sugano, Y. Tanabe, and H. Kamimura, *Multiplets of Transition Metal Ions* (Academic Press, New York, 1970).
- <sup>40</sup>G. Peng, F.M.F. Degroot, K. Hamalainen, J.A. Moore, X. Wang, M.M. Grush, J.B. Hastings, D.P. Siddons, W.H. Armstrong, O.C. Mullins, and S.P. Cramer, *J. Am. Ceram. Soc.* **116**, 2914 (1994).
- <sup>41</sup>P.W. Anderson, *Phys. Rev.* **124**, 41 (1961).
- <sup>42</sup>L.F. Mattheiss, *Phys. Rev. B* **5**, 290 (1972).
- <sup>43</sup>J.C. Slater, *Phys. Rev.* **36**, 57 (1930).
- <sup>44</sup>D.J. Nagel, *Adv. X-Ray Anal.* **183**, 182 (1970).
- <sup>45</sup>K. Okada, A. Kotani, and B.T. Thole, *J. Electron Spectrosc. Relat. Phenom.* **58**, 325 (1992).
- <sup>46</sup>U. Bergmann and S.P. Cramer, *Proceedings of SPIE* (SPIE, San Diego, 1998), Vol. 3448.
- <sup>47</sup>P. Kuiper, B.G. Searle, P. Rudolf, L.H. Tjeng, and C.T. Chen, *Phys. Rev. Lett.* **70**, 1549 (1993).
- <sup>48</sup>A.E. Bocquet, T. Mizokawa, T. Saitoh, H. Namatame, and A. Fujimori, *Phys. Rev. B* **46**, 3771 (1992).